

Laboratory Experiments on Internal Solitary Waves in Ice-Covered Waters

Magda Carr¹, Peter Sutherland², Andrea Haase³, Karl-Ulrich Evers⁴, Ilker Fer⁵, Atle Jensen⁶, Henrik Kalisch⁷, Jarle Berntsen⁷, Emilian Părău⁸, Øyvind Thiem⁹, Peter A. Davies¹⁰

¹School of Mathematics, Statistics & Physics, Newcastle University, Newcastle upon Tyne, NE1 7RU, UK.

²IFREMER, Univ. Brest, CNRS, IRD, Laboratoire d'Océanographie Physique et Spatiale (LOPS), IUEM, Brest, France.

³HSVA, Hamburgische Schiffbau-Versuchsanstalt GmbH, Bramfelder Straße 164, D-22305 Hamburg, Germany.

⁴solutions4arctic, Sommerpfad 2, D-22395 Hamburg, Germany.

⁵Geophysical Institute, University of Bergen, Postboks 7803, 5020 Bergen, Norway.

⁶University of Oslo, Postboks 1053, Blindern, 0316 Oslo, Norway.

⁷Department of Mathematics, University of Bergen, Postboks 7803, 5020 Bergen, Norway.

⁸School of Mathematics, University of East Anglia, Norwich, UK.

⁹Norwegian Public Roads Administration, Bergen, Norway.

¹⁰Department of Civil Engineering, University of Dundee, Dundee, DD1 4HN, UK.

Key Points:

- Internal solitary waves in partially ice-covered water are generated in the laboratory.
- Internal solitary wave induced currents can transport the ice horizontally.
- **In the laboratory experiments**, dissipation of turbulent kinetic energy under the ice is comparable to that at the wave density interface.

Corresponding author: M. Carr, magda.carr@newcastle.ac.uk

Abstract

Internal solitary waves (ISWs) propagating in a stably-stratified two-layer fluid in which the upper boundary condition changes from open water to ice are studied for cases of grease, level and nilas ice. The ISW-induced current at the surface is capable of transporting the ice in the horizontal direction. In the level ice case, the transport speed of, **relatively long ice floes**, non-dimensionalised by the wave speed is linearly dependent on the length of the ice floe non-dimensionalised by the wave length. Measures of turbulent kinetic energy dissipation under the ice are comparable to those at the wave density interface. Moreover, in cases where the ice floe protrudes into the pycnocline, interaction with the ice edge can cause the ISW to break or even be destroyed by the process. The results suggest that interaction between ISWs and sea ice **may be an** important mechanism for dissipation of ISW energy in the Arctic Ocean.

1 Introduction

Internal waves (IWs) are ubiquitous in stratified water. They propagate through the stratified water column and, in the case of a two-layer fluid, along the density interface. In the Arctic Ocean, IW dynamics (i) constitute an integral part of the circulation and thermodynamics (Levine, Paulson, & Morison, 1985; Sandven & Johannessen, 1987), and (ii) play an important role in the vertical mixing of the upper layers (D’Asaro & Morison, 1992; Fer, 2014; Kirillov, 2006) which, in turn, affects renewal of nutrients and sea ice evolution.

The majority of past observations have been of low-frequency IWs, based on sparse *in situ* measurements due to year-round sea ice cover. Recently, however, as a consequence of prolonged ice retreat, synthetic aperture radar (SAR) observations have facilitated the mapping of high-frequency internal solitary waves (ISWs) in open water areas of the Arctic Ocean and its marginal seas (Kozlov et al., 2015; Kozlov, Zubkova, & Kudryavstev, 2017; Zimin, Kozlov, Atadzhanova, & Chapron, 2016). The waves are typically non-linear, rank-ordered packets in which the leading wave has an amplitude that is comparable to the upper layer depth.

A dominant generator of IWs is tidal flow over topography, where the energy of the surface tide is converted to the internal (baroclinic) tide, typically at semidiurnal frequencies. For most of the major tidal constituents, the Arctic is above the critical latitude where the propagation of linear IWs is suppressed by the Earth’s rotation. Yet, IWs have been observed in the Arctic Ocean, associated with increased turbulence (Padman & Dillon, 1991; Rippeth et al., 2017). The mechanisms of generation and energy pathways to turbulence are not yet fully understood. The frequency of the IW packets and their characteristic spatial scales suggest that the majority are linked to the barotropic tide and are a consequence of a lee wave generation process first proposed by Vlasenko, Stashchuk, Hutter, and Sabinin (2003). Recent idealized modelling and field observations (Rippeth et al., 2017) have supported the lee wave generation process and have linked such non-linear IWs to enhanced mixing through collocated velocity microstructure measurements.

Enhanced levels of dissipation of turbulent kinetic energy (TKE) are well documented over areas of sloping topography in the Arctic Ocean (D’Asaro & Morison, 1992; Fer, Skogseth, & Geyer, 2010; Padman & Dillon, 1991; Rainville & Winsor, 2008; Rippeth, Lincoln, Green, Sundfjord, & Bacon, 2015). This is in contrast to the central Arctic Ocean, which is remarkably quiescent (Fer, 2009; Lincoln et al., 2016) **and has shown a lack of significant long-term trends despite changes in sea ice concentration (Guthrie, Morison, & Fer, 2013)**. By synthesizing a pan-Arctic data set Rippeth et al. (2015) suggest tidal conversion as the main source of enhanced dissipation rates and vertical heat fluxes, despite much of the Arctic Ocean lying poleward of the critical latitude. Short scale IWs (which are not affected by the Earth’s rotation) have been proposed as the agency re-

75
76

responsible for the transfer of energy from the tide to turbulent mixing at such latitudes (Rippeth et al., 2017).

77
78
79
80
81
82
83
84

IWs are known to cause flexure of sea ice (Czipott et al., 1991; Marchenko, Morozov, Muzylev, & Shestov, 2010) and theoretical studies (Muench, LeBlond, & Hachmesiter, 1983; Saiki & Mitsudera, 2016) suggest they are responsible for the formation of ice bands in the marginal ice zone (MIZ). The annual variation of the Arctic ice edge is monitored carefully (i) to assess climate change and (ii) for a variety of practical reasons involving sea traffic, fisheries, offshore operations and military marine activities. There is clear interplay between IWs and sea ice and motivation to study the topic is wide ranging, yet very few dedicated investigations exist.

85
86
87
88
89
90
91
92
93
94
95
96
97
98
99
100
101

While field observations provide insight into IW dynamics in the Arctic Ocean, none to date isolate the effects of individual ice, ocean and wind parameters. Moreover, field measurements in the MIZ are particularly challenging and hazardous due to variable ice thickness, and high potential for ice floe breakup. In addition, the harshness of the environment and the remoteness of the location can limit observations, especially in periods of ice-cover. SAR imagery has provided valuable new insight but its use is restricted to areas of open water and to climatic conditions being favourable for the observations to be made. There is a clear need, therefore, to supplement field work with modelling studies. In this study, a laboratory investigation of ISWs in a two-layer stratified flow propagating from open water to under ice is presented. The ice type is varied and the interaction between the ISW and ice investigated. The aim of the paper is to model physically the interaction of an ISW with different types of ice and hence demonstrate that this interaction can lead to dissipation of ISW energy through different pathways including (i) boundary friction at the underside of the ice, (ii) transportation of the ice and (iii) deformation of the wave form. The study is primarily illustrative and qualitative; a full sweep of parameter space being beyond the scope of the current paper. This is the first time that ISWs have been generated under ice in a laboratory setting.

102
103

2 Experimental Set Up and Procedure

2.1 Physical Arrangement and Wave Generation

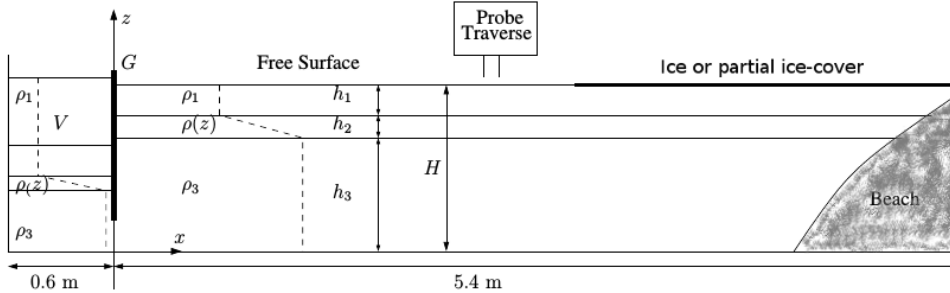


Figure 1. Schematic diagram (not to scale) of the laboratory arrangement.

104
105
106
107
108
109
110
111

The experiments took place in a wave flume 6m in length, 0.47m in width and 0.6m in depth. The flume was built within the HSVA Arctic Environmental Test Basin facility in Hamburg. The flume was of plexiglass construction to allow visualisation from the side and illumination from below. It was filled with homogeneous salt water of prescribed density $\rho_3 = 1045 \text{ kg/m}^3$. Less dense brine solution of density $\rho_1 = 1025 \text{ kg/m}^3$ was then slowly added via an array of floating surface sponges. Consequently, an interface (pycnocline) between the two fluids formed in which the density varied as a linear function of depth z . The density range was chosen such that neutrally-buoyant particles could

112 be suspended throughout the depth of the water column enabling flow visualisation and
 113 measurement (see §2.4). A gate G , was inserted at the upstream end of the tank (see
 114 fig 1) and lowered to approximately 1 cm above the bed of the flume. A fixed volume,
 115 V , of water of density ρ_1 was then added behind the gate. Due to hydrostatic balance,
 116 fluid of density ρ_3 flowed under the gate into the main section of the flume. Once the
 117 volume, V , had been added, the total fluid depth H , in the main section of the flume,
 118 was measured using a pre-set tape on the plexiglass window. The laboratory air tem-
 119 perature was kept just above 0°C while the flume was filled.

120 2.2 Ice Formation

121 After the flume had been stratified, different ice cover types were applied. A vast
 122 array of ice types can be found in the Arctic Ocean hence the ice types investigated were
 123 chosen to cover as broad a range as practically possible. The laboratory was cooled to
 124 approximately -2°C or -15°C in cases where ice was added or made respectively. The
 125 temperature and thickness of the ice was monitored throughout the duration of a given
 126 experiment. No change of form or melting was observed.

127 (i) **Model level ice** was formed from a 0.7% sodium chloride solution following
 128 the procedure outline in Evers (2015). During the freezing process tiny air bubbles of
 129 diameter 200–500 μm were embedded into growing ice crystals. Due to the embedded
 130 air, the mechanical properties of the model ice (strength, elasticity, fracture behaviour
 131 and density) were made as close as possible to the mechanical properties of ice prevail-
 132 ing in nature. In particular, the model ice had a density range of 782–803 kg/m^3 which
 133 is within the natural range for sea ice of 720–940 kg/m^3 . Sections of level ice were cut
 134 and removed from the laboratory and kept in a cold storage unit. When required, the
 135 floes of level ice were carefully lowered into the stratified flume. **The level ice floes had**
 136 **a length, $l_f \approx 1$ m, and two different thicknesses were considered namely $d_f = 0.013$**
 137 **m and $d_f = 0.058$ m.**

138 (ii) **Grease ice** was made by crushing stored model level ice and adding it care-
 139 fully to the surface of the stratified water while taking care to disturb neither the py-
 140 cnocline nor the upper layer. **Individual pieces of grease ice had complex geometries and**
 141 **the typical length scale of a piece ranged from 0.001 m to 0.05 m. These pieces were ar-**
 142 **ranged such that a surface length of 2.65 m was covered by the ice and the total thick-**
 143 **ness of the grease ice layer was approximately 0.02 m.**

144 (iii) **Nilas ice** was made by reducing the air temperature in the laboratory (to -15°C)
 145 so that the surface of the water column froze. Open water sections were maintained by
 146 placing styrofoam at the surface during the freezing process. The styrofoam lids were
 147 removed just prior to an experiment commencing. **The thickness of the nilas ice layer**
 148 **was approximately 0.006 m and it covered a surface length of 2.69 m.**

149 2.3 Wave Generation

150 ISWs were generated by the swift, smooth removal of the gate in the vertical di-
 151 rection. After a sorting distance of approximately 1 m, an ISW of depression propagated
 152 horizontally along the pycnocline into the main section of the tank. A beach (of polyether
 153 filter foam) was located at the downstream end of the flume to absorb some of the ISW
 154 energy but a reflected ISW signal was still seen in all but one of the experimental runs.
 155 Once an experiment was finished and the water column stationary, the gate was re-inserted
 156 and a fixed volume of fluid of density ρ_1 was again added behind the gate so that a sec-
 157 ond run could be performed.

2.4 Flow Measurement and Flow Visualisation

With the ice in place and the water column stationary, high precision micro-conductivity sensors (Munro & Davies, 2009) were used to measure the form of the stratification. The sensors were mounted on a rigid rack and pinion traverse system fitted with a potentiometer. The sensors were moved vertically through the water column and density profiles were obtained by calibrating the potentiometer output and conductivity data against known values of height and fluid density respectively.

Analysis was restricted to two dimensions, (x, z) , where x denotes the horizontal direction and z the vertical direction, with the origin $x = 0$ corresponding to the horizontal location of the gate and $z = 0$ to the bed of the flume (see fig 1). The vertical extent of the upper, middle and lower layers of the stratification were denoted by h_1, h_2 and h_3 respectively. The ratio of the layer thicknesses, and in particular the upper two layer thicknesses, were chosen to be similar to those observed in the Eurasian Arctic shelf seas and slopes (Fer et al., 2010; Kozlov, Romanenkov, Zimin, & Chapron, 2014; Padman & Dillon, 1991). The formation of the stratification was difficult to control precisely due to (i) disturbances during filling, (ii) disturbances when adding the ice and (iii) differences in filling times. As a result the layer depths varied such that, $h_3 = 0.32 \pm 0.01$ m, $h_2 = 0.04 \pm 0.01$ m and $h_1 = 0.045 \pm 0.002$ m for the first run of a given experiment, and $h_3 = 0.32 \pm 0.01$ m, $h_2 = 0.04 \pm 0.01$ m and $h_1 = 0.055 \pm 0.002$ m for the second run.

A light source (intense LED strip passed through a double slit), was placed beneath the transparent base of the tank. It generated a thin, vertical column of light which was arranged to illuminate a two dimensional slice of the flow field in the mid-plane of the flume aligned with the x axis. The water column was seeded with neutrally-buoyant, light-reflecting tracer particles of "Pliolite" having diameters in the range 150–300 μm (Fructus, Carr, Grue, Jensen, & Davies, 2009). Motions within the vertical light sheet were viewed and recorded from the side using three fixed digital video cameras set up outside the flume. The cameras (UNIQ UP-1830-CL-12B) had a spatial resolution of 1372×1372 pixels and a capture rate of 30 frames per second. The three cameras were synchronised in time and two were positioned to have overlapping fields of view.

The software package *DigiFlow* (Dalziel, Carr, Sveen, & Davies, 2007) was used to process the digital video records. The time series function of *DigiFlow* was used to measure wave phase speed c , wave amplitude a , wave length λ and wave-induced ice floe speed c_f . The Particle Image Velocimetry (PIV) function of *DigiFlow* was used to calculate continuous synoptic velocity and vorticity field data along the illuminated cross-section in the middle of the flume. The average ice thickness d_f and ice length l_f were measured with calipers and a rule respectively. The width of the ice was as close as practically possible to the width of the tank.

3 Results

3.1 Ice Motion

Provided the ice was free to move, the ISW-induced current at the surface transported the ice horizontally in the same direction as that of wave propagation. This is illustrated in figure 2 (a) in which still images from an experiment with level ice of dimensions $d_f = 0.013\text{m}$ and $l_f = 0.95\text{m}$ are presented. The images show light scattered from the neutrally-buoyant tracer particles and are displayed in a false colour scheme to optimise the visualisation. The ice at the surface can be seen by light reflected off its underside and the pycnocline can be identified by the clustering of tracer particles at the density interface. The ISW propagated from left to right.

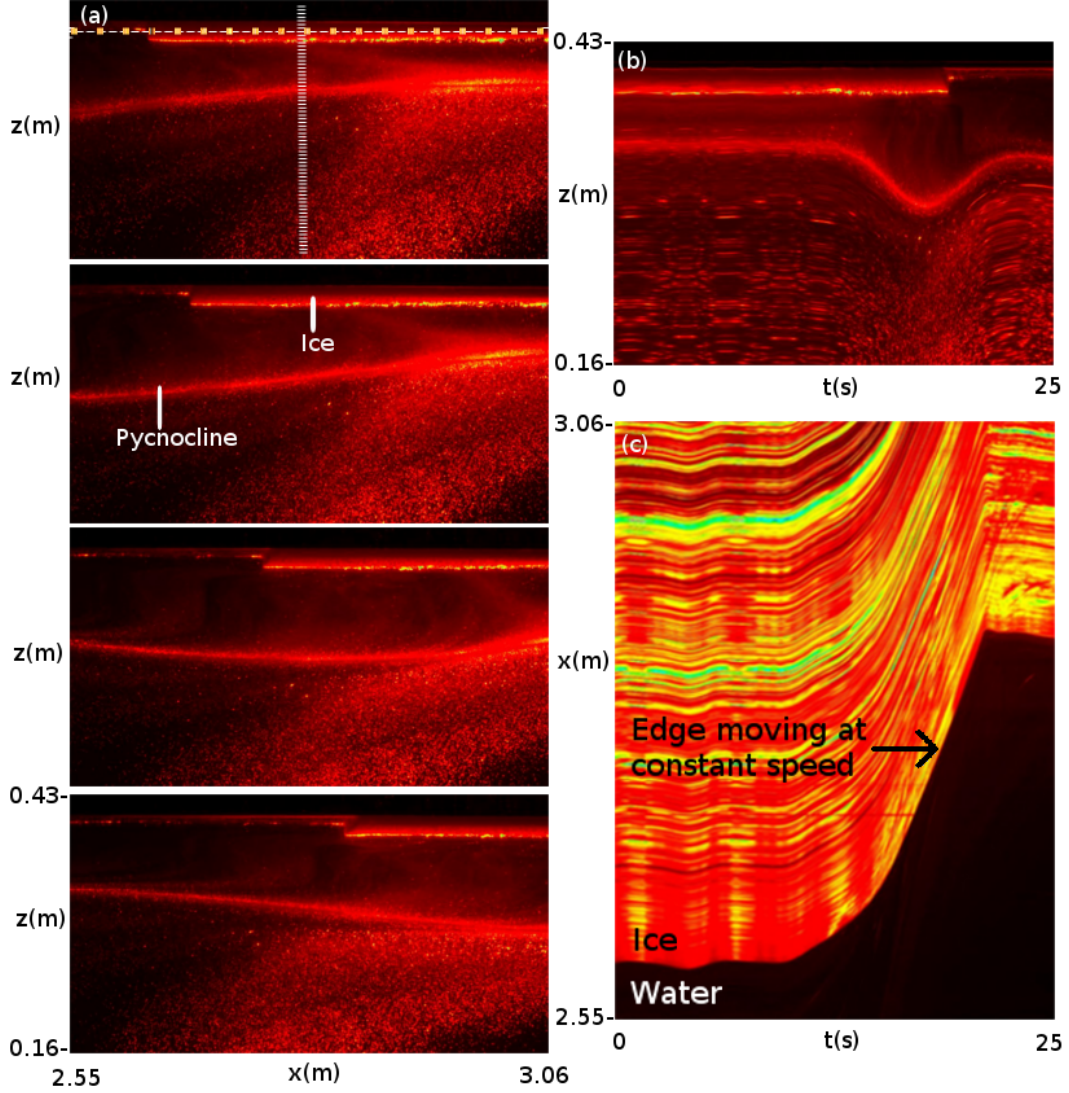


Figure 2. (a) series of still experimental images with level ice of dimensions $d_f = 0.013\text{m}$ and $l_f = 0.95\text{m}$, showing light intensity, ordered sequentially in time from top to bottom at intervals of $\Delta t=2.2\text{ s}$, (b) vertical time series made from column marked by vertical dashed line in (a), and (c) horizontal time series made from row marked by horizontal dot-dashed line in (a) rotated through 90° anticlockwise.

206 Figure 2 (b) shows a time series constructed by measuring the temporal changes
 207 in image pixel values in a prescribed column at a fixed horizontal coordinate in each frame
 208 of the experimental movie over a time interval of 25 s. Such series were used to measure
 209 wave amplitude by tracing the vertical disturbance of a streamline at the top ($z = h_3 +$
 210 h_2) of the pycnocline from its undisturbed depth to maximal displacement. The time
 211 at which the pycnocline reached maximum displacement was also recorded. This process
 212 was repeated at three fixed locations $x_{1,2,3}$ over known horizontal distances $\delta x \approx$
 213 0.26 m . The wave phase speed $\delta x / \delta t$ was obtained by noting the time δt between
 214 maximal interface displacement at the three fixed locations $x_{1,2,3}$. This process was repeated
 215 over all three cameras for waves in which there was no change of form. Average amplitude
 216 a and average wave phase speed c were then computed. The half wavelength, λ , was

217 calculated from the time series by measuring the time taken for the pycnocline to be dis-
 218 placed from $z = h_3 + h_2 - a/2$ to $z = h_3 + h_2 - a$, to get a quarter wavelength and
 219 then multiplying the result by $2c$.

220 Figure 2 (c) shows a time series constructed by measuring the temporal changes
 221 in image pixel values in a prescribed row of lateral extent $x \in [2.55, 3.06]$ m at a fixed
 222 vertical coordinate in each frame of the experimental movie, over a time interval of 25
 223 s. The horizontal slices (which coincide with the ice) are rotated through 90° anticlock-
 224 wise and ordered sequentially from left to right. In this way the edge of the ice (marked
 225 by the interface between black and orange) can be traced. It can be seen that after an
 226 initial acceleration (due to the wave motion c.f. fig 2 (b)) the ice moves at a constant
 227 speed before it encounters the end of the wave flume and is arrested. The constant floe
 228 speed, c_f , was measured from the gradient of the straight section of the trace indicated
 229 by an arrow in fig 2 (c).

230 Figure 3 (a) summarises the range of wave phase speeds, wave amplitudes, ice types
 231 and dimensions investigated (see supplementary table for further details). In figure 3 (b)
 232 the non-dimensional floe speed c_f/c versus the non-dimensional ice floe length $l_f/2\lambda$ is
 233 presented for the level ice cases only. In these cases, the ice floe was relatively long, $l_f/d_f \in$
 234 $[17.2, 73.1]$ and completely free to move. In the grease ice case, the ice was not packed
 235 in tight and there were regions where it was possible to compress the ice but the ice ini-
 236 tially extended to the end wall of the flume and hence was only partially free to move
 237 in the horizontal direction. Nevertheless, the wave-induced flow transported the grease
 238 ice horizontally (at a speed of $c_f/c \approx 0.25$). In the case of the nilas ice, the ice was fixed
 239 in the positive horizontal direction (by the end wall of the flume) and hence there was
 240 no wave-induced floe movement. Figure 3 (b) suggests that when the ice is free to move
 241 and the floe is relatively long, there is a linear relationship between the wave-induced
 242 floe speed and the floe length given by the equation of the plotted straight line, namely,
 243 $c_f/c = -0.61l_f/2\lambda + 0.79$. The wave-induced floe speed was not found to have any de-
 244 pendence on the thickness of the ice floe d_f for the parameter range investigated ($d_f \in$
 245 $[0.013, 0.058]$ m).

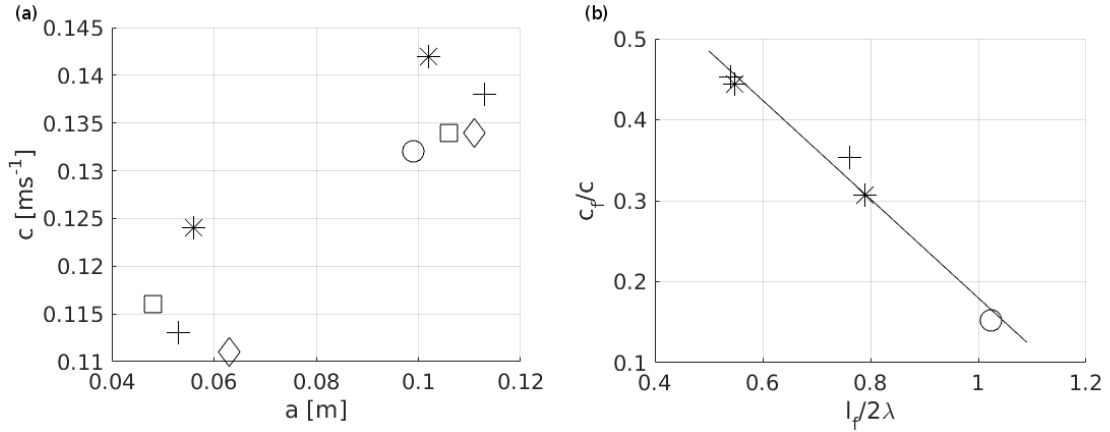


Figure 3. (a) Wave phase speed c versus wave amplitude a and (b) non-dimensional wave-induced level ice floe speed c_f/c versus non-dimensional level ice floe length $l_f/2\lambda$. Different symbols correspond to different ice types and dimensions as follows: * level ice with $d_f = 0.013$ m and $l_f = 0.95$ m, + level ice with $d_f = 0.058$ m and $l_f = 1.00$ m, o level ice with $d_f = 0.058$ m and $l_f = 2.00$ m, ◇ grease ice with $d_f = 0.021$ m and $l_f = 2.65$ m, □ nilas ice with $d_f = 0.006$ m and $l_f = 2.69$ m. The solid straight line in (b) is a linear fit (with $R^2 = 0.982$) to the data points. Error bars are omitted from the data points as they were comparable with the marker size.

246

3.2 Wave/Ice Edge Interaction

247

248

249

250

251

252

253

In figure 4, still images from two experiments in which the ice protruded into the pycnocline are presented. The sub-panels are constructed from two overlapping camera outputs. In the smaller wave amplitude case (figure 4 (a)), the interaction of the wave with the ice edge caused deformation of the wave shape (figure 4 (a), (ii)-(iv)) and the wave amplitude was significantly reduced (figure 4 (a), (v)), so much so that in this case there was no reflected wave signal off the end wall of the flume. The wave was effectively destroyed by its interaction with the ice edge.

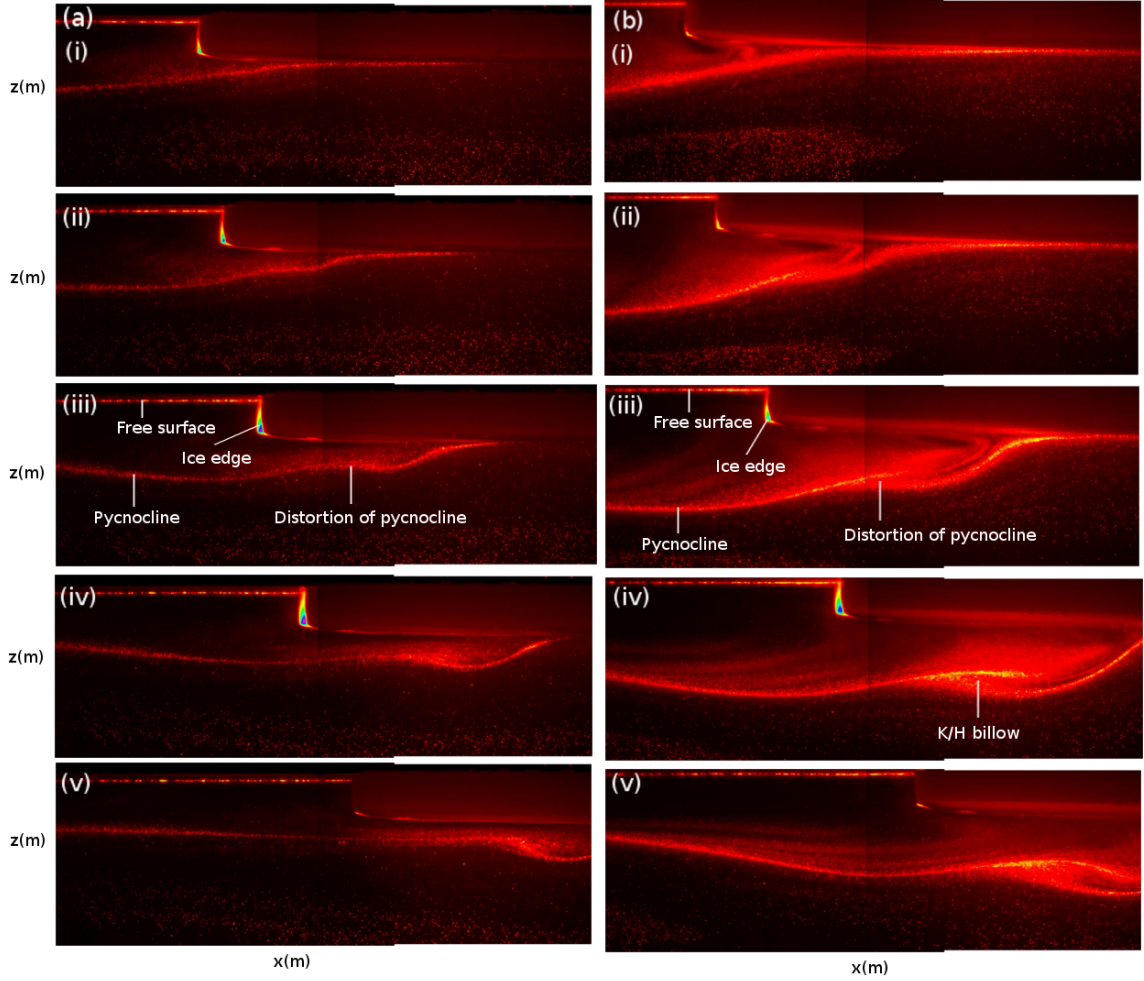


Figure 4. Series of experimental images for an experiment in which the ice was level ice of dimensions $d_f = 0.058\text{m}$ and $l_f = 1.00\text{m}$, and the incident ISW had (a) $a = 0.053\text{ m}$ and (b) $a = 0.113\text{m}$. The images show light intensity and ordered sequentially in time from top to bottom at intervals of $\Delta t = 2.14\text{ s}$; sub-panel dimensions are $(\Delta x, \Delta z) \approx (0.813\text{m}, 0.74\text{m})$. The ISW propagates from left to right.

254

255

256

257

258

259

In the larger wave amplitude case (figure 4 (b)), interaction of the wave with the ice edge caused similar deformation of the wave shape, to the smaller amplitude case but this time a billow resembling the overturning features associated with a Kelvin-Helmholtz instability (Fructus et al., 2009) occurred on the pycnocline (see figure 4 (b), (iv) & (v)). Note that the dynamics in the two cases were similar but the proximity of the ice to the pycnocline in case (a) impeded clear billow formation.

260

3.3 Dissipation of Turbulent Kinetic Energy Under the Ice

261

262

263

264

265

266

267

268

269

270

271

272

273

274

275

276

The three different ice types had different topographic features and associated roughness on their undersides. For example, the grease ice was lumpy in structure and the nilas ice grew columnar ice crystals down into the water, whereas the underside of the level ice was flat and relatively smooth. In figure 5, fields of horizontal velocity, u , vorticity, ω , dissipation of TKE, ϵ , and profiles of horizontally averaged TKE dissipation, $\bar{\epsilon}$, are presented for experiments with comparable wave amplitudes and wave shape but under varying ice types. The velocity and vorticity field were computed via PIV. TKE dissipation was computed from the PIV velocity fields following the direct gradient method given in Doron, Bertuccioli, Katz, and Osborn (2001), using 64×64 point, 75% overlapping, estimation windows. This estimate of dissipation requires the assumption that cross-plane velocity gradients have the same average magnitude as the measured in-plane velocity gradients. This estimate also assumes that the spatial resolution of the measured velocity fields is smaller than, or comparable to, the Kolmogorov scale, which was true in all cases presented here. The mean TKE dissipation, $\bar{\epsilon}$, was calculated by horizontally averaging the dissipation at every depth bin over the region plotted (minus a small section of width 0.1m at each side).

277

278

279

280

281

282

283

284

285

286

287

288

289

290

291

292

293

294

295

296

297

298

299

300

301

The approximate location of the underside of the ice and the top of the pycnocline were attained by analysing regions of light intensity in the experimental images. The horizontal velocity plots confirm the findings in §3.1 i.e. the grease ice and level ice were transported horizontally by the wave-induced flow. Enhanced vorticity is seen under the nilas ice when compared with the other cases. This is presumably because the nilas ice was stationary and hence the velocity gradient close to the ice, du/dz , is biggest in this case. Moreover, the vorticity plots show that the vertical extent of the vorticity layer directly under the ice is larger in the nilas and grease cases than the level case. This can be attributed to the relatively larger roughness of the grease ice and nilas ice compared to the level ice. Indeed in these cases, small vortices were seen to form at the underside of the ice downstream of any rough features. The TKE dissipation plots show (in all 3 cases) that dissipation levels under the ice are comparable with dissipation levels at the pycnocline, suggesting a mechanism for increased IW dissipation and consequently reduced propagation in the ice-covered Arctic Ocean. The mean TKE dissipation profiles confirm that there is a peak in the TKE dissipation below the ice and at the pycnocline. Integration of the TKE dissipation over these two regions of enhanced TKE dissipation give the near-ice dissipation as 77%, 64%, and 54% of the pycnocline value in the grease, nilas, and level ice cases respectively. Or in other words, dissipation near the ice accounts for approximately 44%, 39%, and 35%, of the total dissipation due to turbulence in the grease, nilas, and level ice cases respectively. The elevated TKE dissipation under the nilas and grease ice hypothesize that a rougher ice bottom and increased vertical shear of horizontal velocity lead to higher TKE dissipation in the upper boundary layer. Note that the TKE dissipation measures presented here are true for the experimental conditions tested, whether similar characteristics are seen in the field remains an open question.

302

4 Relevance to the Field

303

304

305

306

307

308

The interaction of ISWs with an ice edge are expected to be an effective mechanism of dissipating ISW energy and causing localised turbulence and mixing in the field. Similar dissipation is expected beneath any structures (e.g. ice ridge keels or rafted ice) that protrude into the pycnocline. In the field, vortex formation at the underside of the ice surface is expected to contribute further to dissipation of kinetic energy in a similar way to that found at the bottom boundary of the ocean.

309

310

The parameter space considered was limited by physical constraints. It differed from the ocean in both Reynolds number, $Re = ac/\nu$ (where ν is kinematic viscosity) and

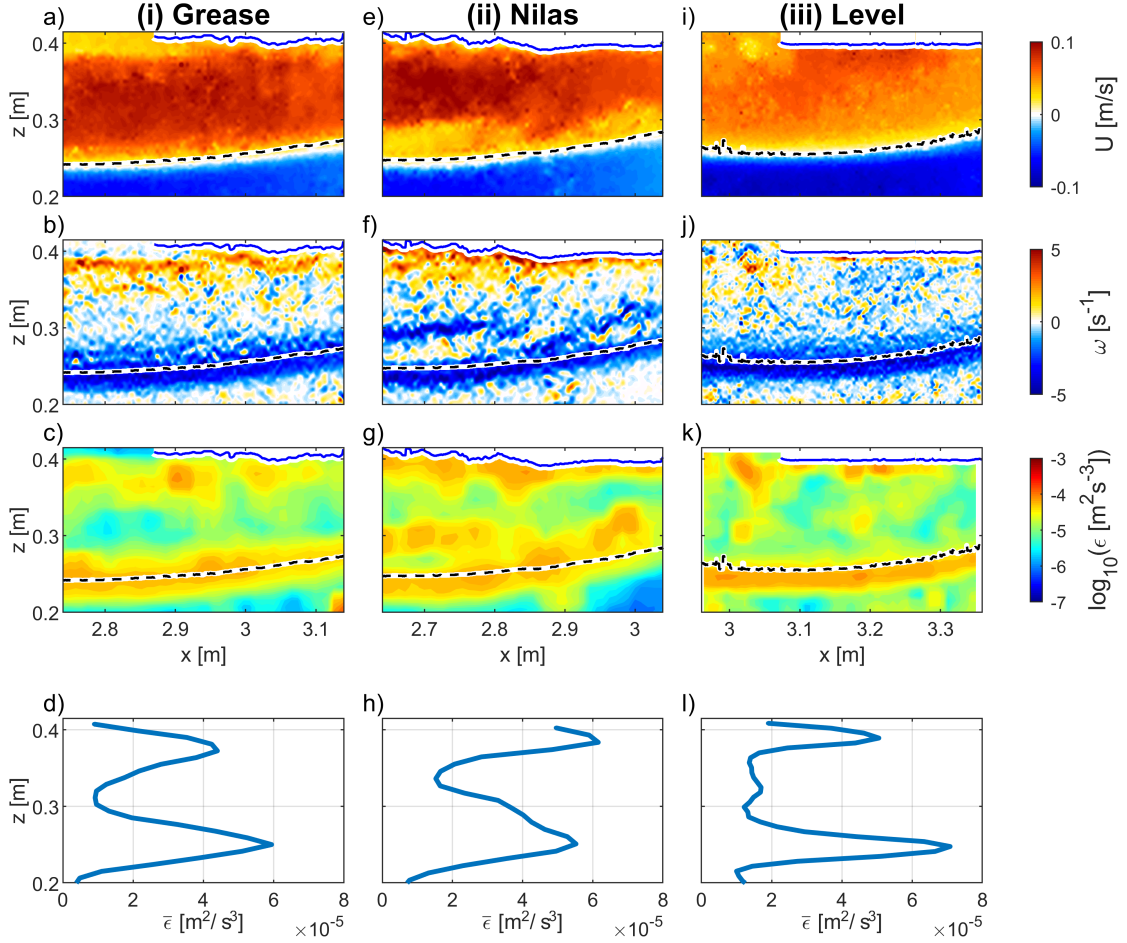


Figure 5. PIV measurements of (a, e, i) horizontal velocity u (ms^{-1}), (b, f, j) vorticity ω (s^{-1}), and corresponding calculations of (c, g, k) TKE dissipation $\log_{10}(\epsilon$ (m^2s^{-3})), and (d, h, l) mean TKE dissipation $\bar{\epsilon}$ (m^2s^{-3}) under (i) grease ice (a-d), (ii) nilas ice (e-h) and (iii) level ice (i-l). The black dashed line and the solid blue line depict the top of the pycnocline and the underside of the ice respectively.

311 buoyancy frequency

$$N = \sqrt{\frac{-g}{\rho_0} \frac{\partial \rho}{\partial z}}, \quad (1)$$

312 where g is acceleration due to gravity and ρ_0 is some reference density. Re and N in the
 313 laboratory were of the order 10^3 and 1 s^{-1} respectively. In the Arctic Ocean, when strat-
 314 ification is at its strongest, corresponding values are of the order 10^6 and 0.01 s^{-1} , re-
 315 spectively. Hence, to understand whether the laboratory results scale to the ocean re-
 316 quires variation of Re and N in the future. Moreover, study over a wider range of d_f/h_1
 317 and $l_f/2\lambda$ would provide better insight into field scale dynamics.

318 The wave phase speed, c , in the experiments was $O(0.1) \text{ ms}^{-1}$ and is comparable
 319 to field values which are typically $0.2\text{--}0.5 \text{ ms}^{-1}$ in the Arctic Ocean. The experiments
 320 were conducted in a flume at rest, hence an inference regarding Froude number, Fr , (ra-
 321 tio of inertia to the external gravity field) is not relevant. The experiments can, how-
 322 ever, be compared to nonlinear lee waves in the field (Rippeth et al., 2017) once the ini-

323 tially trapped and steepened wave (which has a $Fr \approx 1$) is released and allowed to prop-
 324 agate in sub-critical conditions ($Fr < 1$).

325 5 Conclusion

326 The ISW-induced current was shown to transport ice horizontally and the trans-
 327 port speed of relatively long ice floes was linearly dependent on the floe length for the
 328 parameter range considered. When the ice protruded into the pycnocline, interaction of
 329 the wave with the ice edge resulted in a Kelvin-Helmholtz billow forming on the pycno-
 330 cline and the resulting wave signal being deformed or destroyed. If the underside of the
 331 ice was rough, boundary layer development due to the ISW-induced flow was observed
 332 and finally it was shown that levels of TKE dissipation under the ice were comparable
 333 to those at the pycnocline. The parameter range investigated was limited by the scale
 334 of the facility but nevertheless the observations show that the physical interactions of
 335 ISWs with ice could have important implications for dissipation of wave energy, and con-
 336 sequent mixing in the polar oceans and point to the need for further more detailed in-
 337 vestigations. Moreover, the observation that an ISW can transport ice horizontally sug-
 338 gests that a series of ISWs may well constitute a mechanism by which sea ice banding
 339 can occur as proposed theoretically by Saiki and Mitsudera (2016).

340 Acknowledgments

341 The work described in this publication was supported by the European Community's
 342 Horizon 2020 Research and Innovation Programme through the grant to HYDRALAB-
 343 PLUS, Contract no. 654110. This work received funding from the MASTS pooling ini-
 344 tiative (The Marine Alliance for Science and Technology for Scotland) and their support
 345 is gratefully acknowledged. MASTS is funded by the Scottish Funding Council and con-
 346 tributing institutions. The authors thank Nis Schnoor and Gesa Zimmer for providing
 347 technical assistance at HSVA, Hamburg and Prof Tom Rippeth (University of Bangor)
 348 for useful discussion of the work. The EPSRC UK Fluids Network is also thanked for
 349 providing funds to disseminate the findings of this work. The data that supports this
 350 work can be accessed at the following DOI: 10.5281/zenodo.2574580. The authors thank
 351 two anonymous referees whose comments have led to improvements in the paper.

352 References

- 353 Czipott, P. V., Levine, M. D., Paulson, C. A., Menemenlis, D., Farmer, D. M., &
 354 Williams, R. G. (1991). Ice flexure forced by internal wave packets in the
 355 Arctic Ocean. *Science*, *254*, 832-835.
- 356 Dalziel, S. B., Carr, M., Sveen, J. K., & Davies, P. A. (2007). Simultaneous syn-
 357 thetic schlieren and PIV measurements for internal solitary waves. *Measure-*
 358 *ment Science and Technology*, *18*, 533-547.
- 359 D'Asaro, E. A., & Morison, J. H. (1992). Internal waves and mixing in the Arctic
 360 Ocean. *Deep Sea Research Part II*, *39*, S459-S484.
- 361 Doron, P., Bertuccioli, L., Katz, J., & Osborn, T. R. (2001). Turbulence characteris-
 362 tics and dissipation estimates in the coastal ocean bottom boundary layer from
 363 PIV. *J. Phys. Oceanogr.*, *31*, 2108-2134.
- 364 Evers, K.-U. (2015). Modeling ice processes in laboratories and determination of
 365 model ice properties. In P. Langhorne (Ed.), *Cold regions science and marine*
 366 *technology*. EOLSS Publishers.
- 367 Fer, I. (2009). Weak vertical diffusion allows maintenance of cold halocline in the
 368 central Arctic. *Atmospheric and Oceanic Science Letters*, *2*, 148-152.
- 369 Fer, I. (2014). Near-Inertial Mixing in the Central Arctic Ocean. *Journal of Physical*
 370 *Oceanography*, *44*, 2031-2049.
- 371 Fer, I., Skogseth, R., & Geyer, F. (2010). Internal waves and mixing in the Marginal

- 372 Ice Zone near the Yermak Plateau. *Journal of Physical Oceanography*, *40*,
373 1613-1630.
- 374 Fructus, D., Carr, M., Grue, J., Jensen, A., & Davies, P. A. (2009). Shear induced
375 breaking of large amplitude internal solitary waves. *Journal of Fluid Mechan-*
376 *ics*, *620*, 1-29.
- 377 Guthrie, J., Morison, J. H., & Fer, I. (2013). Revisiting internal waves and mixing in
378 the arctic ocean. *J. Geophys. Res.*, *118*, 3966-3977.
- 379 Kirillov, S. (2006). Spatial variations in sea-ice formation-onset in the Laptev sea as
380 a consequence of the vertical heat fluxes caused by internal waves overturning.
381 *Polarforschung*, *79*, 119-123.
- 382 Kozlov, I. E., Kudryavstev, V. N., Zubkova, E. V., Atadzhanova, O., Zimin, A. V.,
383 Romanenkov, D., ... Chapron, B. (2015). SAR observations of internal waves
384 in the Russian Arctic Seas. In (p. 947-949). IEEE international.
- 385 Kozlov, I. E., Romanenkov, D., Zimin, A. V., & Chapron, B. (2014). SAR observing
386 large-scale nonlinear internal waves in the White Sea. *Remote Sensing of Envi-*
387 *ronment*, *147*, 99-107.
- 388 Kozlov, I. E., Zubkova, E. V., & Kudryavstev, V. N. (2017). Internal solitary waves
389 in the Laptev Sea: First results of spaceborne SAR observations. *IEEE Geo-*
390 *science & remote sensing letters*, *14*, 2047-2051.
- 391 Levine, M. D., Paulson, C. A., & Morison, J. H. (1985). Internal waves in the Arc-
392 tic Ocean: Comparison with lower-latitude observations. *Journal of Physical*
393 *Oceanography*, *15*, 800-809.
- 394 Lincoln, B. J., Rippeth, T. P., Lenn, Y.-D., Timmermans, M. L., Williams, W. J.,
395 & Bacon, S. (2016). Wind-driven mixing at intermediate depths in an ice free
396 Arctic Ocean. *Geophysical Research Letters*, *43*, 9749-9756.
- 397 Marchenko, A. V., Morozov, E., Muzylev, S. V., & Shestov, A. S. (2010). Interac-
398 tion of short internal waves with ice cover in an Arctic fjord. *Oceanology*, *50*,
399 18-27.
- 400 Muench, R., LeBlond, P. H., & Hachmesiter, L. E. (1983). On some possible inter-
401 actions between internal waves and sea ice in the marginal ice zone. *Journal of*
402 *Geophysical Research*, *88*, 2819-2816.
- 403 Munro, R. J., & Davies, P. A. (2009). The flow generated in a continuously strat-
404 ified rotating fluid by the differential rotation of a plane horizontal disc. *Fluid*
405 *Dynamics Research*, *38* (8), 522-538.
- 406 Padman, L., & Dillon, T. M. (1991). Turbulent mixing near Yermak Plateau during
407 the coordinated eastern Arctic experiment. *Journal of Geophysical Research*,
408 *96*, 4769-4782.
- 409 Rainville, L., & Winsor, P. (2008). Mixing across the Arctic Ocean: Microstructure
410 observations during the Beringia 2005 expedition. *Geophysical Research Let-*
411 *ters*, *35*, L08606.
- 412 Rippeth, T. P., Lincoln, B. J., Green, J. A. M., Sundfjord, A., & Bacon, S. (2015).
413 Tide-mediated warming of Arctic halocline by Atlantic heat fluxes over rough
414 topography. *Nature Geoscience*, *8*, 191-194.
- 415 Rippeth, T. P., Vlasenko, V., Stashchuk, N., Scannell, B. D., Green, J. A. M., Lin-
416 coln, B. J., & Bacon, S. (2017). Tidal conversion and mixing poleward of the
417 critical latitude (an Arctic case study). *Geophysical Research Letters*, *44*,
418 12349-12357.
- 419 Saiki, R., & Mitsudera, H. (2016). A mechanism of ice-band pattern formation
420 caused by the resonant interaction between sea ice and internal waves: A the-
421 ory. *Journal of Physical Oceanography*, *46*, 583-600.
- 422 Sandven, S., & Johannessen, O. M. (1987). High-frequency internal wave observa-
423 tions in the marginal ice zone. *Journal of Geophysical Research*, *92*, 6911.
- 424 Vlasenko, V., Stashchuk, N., Hutter, K., & Sabinin, K. D. (2003). Nonlinear internal
425 waves forced by tides near the critical latitude. *Deep Sea Research. Part I*, *50*,
426 317-338.

427 Zimin, A. V., Kozlov, I. E., Atadzhanova, O. A., & Chapron, B. (2016). Monitor-
428 ing short-period internal waves in the White Sea. *Izvestiya, Atmospheric and*
429 *Ocean Physics*, 52, 951-960.